



N-doped carbonized lignin for electrocatalysts in seawater batteries

Ji Hwan Hong¹ , Inwoo Song¹, Yoonjong Cho, Jinhoon Lee , Jee Ho Ha ,
Myung-Jin Baek , Seok Ju Kang , Dong Woog Lee^{*}

School of Energy and Chemical Engineering, Ulsan National Institute of Science and Technology (UNIST), Ulsan 44919, Republic of Korea

ARTICLE INFO

Keywords:

Seawater battery
Lignin
Urea
Biomass
Electrocatalysts

ABSTRACT

Seawater batteries utilizing naturally abundant seawater as the cathode material offer economic advantages. Despite their versatility, they suffer from slow kinetics and high overpotential, limiting their efficiency. Addressing this, electrocatalysts emerge as crucial for enhancing performance. However, conventional electrocatalysts, primarily noble metals, are scarce and expensive. In this context, carbon materials derived from bio-waste have garnered considerable attention. In this work, we employed lignin, the most abundant aromatic polymer, as a precursor for carbon materials, addressing the critical need for sustainable and efficient electrocatalysts in seawater batteries. To enhance the catalytic properties, we innovatively used urea – a compound typically associated with environmental challenges – for nitrogen doping. This approach allowed us to synthesize doped carbon catalysts that achieved performance metrics comparable to those of conventional Pt/C catalysts. Our findings not only demonstrate the potential of lignin and urea as effective electrocatalysts but also highlight a significant advancement towards enhancing the performance of seawater batteries. This opens new avenues for the development of sustainable energy storage solutions, leveraging biowaste materials to address environmental and energy challenges.

1. Introduction

The urgent need to shift from fossil fuels to renewable energy sources is a significant challenge facing humanity, crucial for addressing global warming and climate change. As the integration of renewable energies into the grid increases, so does the demand for efficient and sustainable energy storage systems (ESS). While lithium-ion batteries (LIBs) have emerged as the dominant technology in the ESS landscape, their widespread adoption is hampered by rising costs [1–7] and environmental concerns associated with lithium extraction, notably its significant freshwater consumption [8–10].

In this context, seawater batteries (SWBs) (Fig. 1), a type of sodium-air battery leveraging the abundance of seawater [11], emerge as a promising alternative. These batteries offer several advantages, including eco-friendliness, potential cost reductions, and higher theoretical energy densities (~4057 Wh/kg) [12,13]. Furthermore, they present opportunities for innovative applications such as Na harvesting [14], desalination [15], and H₂ storage [16].

Seawater batteries utilize seawater as a cathode capable of supplying Na ions for repeated charge–discharge cycles. The oxygen evolution

reaction (OER) occurs upon charging, whereas the oxygen reduction reaction (ORR) takes place during discharging on the carbon-based cathode current collector [17,18]. However, the practical realization of seawater batteries is hindered by challenges such as the slow kinetics of the OER and ORR at the cathode current collector [19–21]. To address these kinetic limitations in the oxygen-involved reactions, electrochemical catalysts must be employed [22]. Noble metals such as Pt, Ir, and Ru are commonly used as catalysts [23–27], but their scarcity and high cost pose significant disadvantages [26,28–31]. In efforts to replace expensive noble metal-based catalysts [32–34], researchers have been exploring various carbon nanomaterial-based catalysts, including fullerene [35], carbon nanotube [36], graphene [37], graphene oxide [38], and graphite [39]; however, these alternatives have safety concerns. Common methods for producing carbon nanomaterials include chemical vapor deposition, often using methane as a reactant and generating H₂ as a byproduct, posing a safety risk during the production process [40]. Furthermore, it does not fully address the issue of cost, since acetylene, xylene, and methane are often used for starting materials, which are expensive carbon feedstocks [41]. To overcome these challenges, research has explored the use of diverse biowaste materials,

^{*} Corresponding author.

E-mail address: dongwoog.lee@unist.ac.kr (D.W. Lee).

¹ These authors contributed equally to this work.

such as grapefruit peel [17], fallen leaves [42], chicken feathers [43], and lignin [44], as carbon precursors.

Specifically, lignin is the most abundant aromatic polymer in nature [45], which is generated as a byproduct in the paper-making and bio-ethanol manufacturing processes. Despite its widespread availability, lignin's complex structure and diverse functional groups have limited its utilization [46–48]. Current applications are largely limited to burning for heat energy, emitting not only CO₂ but also toxic substances [49,50]. Lignin has a great advantage over the abovementioned biowastes in its stable supply. Worldwide, pulp & paper industry generates around 100 million tons of lignin per year [51]. Lignin has shown potential in various fields such as chemical [52], adhesives [53], and biomedical application [54], attracting the attention of researchers. Research on carbonizing lignin and applying it to different applications has also been performed, including water treatment [55], carbon fiber synthesis [56], and energy-related fields including lithium-ion batteries [57] and electric double layer capacitors [58].

It is well-established that introducing a heteroatom significantly enhances catalytic activity [59–61], with nitrogen being a particularly effective candidate. Nitrogen doping is known to induce relatively positive charges on neighboring carbon atoms, owing to differences in electronegativity, thereby increasing the affinity for O₂ adsorption [62,63]. Various nitrogen-containing substances, such as ammonia [64], pyrrole [65], melamine [66], and urea [67] have been explored as dopants.

Urea, produced in the liver of mammals and excreted in the form of urine through the kidneys, is released as effluent from households or agro-breeding industries [68]. Once introduced into ecosystem, urea can transform into substances that contribute to environmental issues such as acid rain and eutrophication [69–71]. Consequently, transforming urea into valuable products represents a crucial strategy for mitigating agricultural waste and reducing pollution [72–74].

In this study, we developed an ORR electrocatalyst (800-NDL), using urea and lignin as the starting biowaste materials. We then utilized 800-NDL at the cathode of a seawater battery, where it demonstrated a lower voltage gap of 0.71 V and achieved a peak power density of 7.9 mW/cm² which is comparable to those of the conventional Pt/C catalysts (0.74 V and 8.1 mW/cm², respectively). These results highlight the potential of 800-NDL as an effective electrocatalyst in sodium-air batteries, emphasizing its suitability for sustainable energy storage solutions.

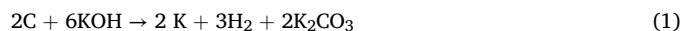
2. Materials and methods

2.1. Carbonization and activation of lignin

Lignin, in its powdered form (Sigma-Aldrich), was carbonized and activated in a single-step process. 3 g of lignin and 12 g of potassium

hydroxide (KOH, SAMCHUN) were dissolved in 30 mL of distilled water. The solution was then completely dried at 80 °C for 12 h in a convection oven. The dried mixture was subsequently placed in an alumina crucible for heat treatment within an electric tube furnace under an argon atmosphere. The temperature was ramped up to the target activation temperatures of 600 °C, 800 °C, or 1000 °C at a rate of 10 °C/min. Upon reaching the target temperature, it was maintained for 2 h to ensure complete activation.

The activation process of carbon by KOH is reported as follows [75].



The resulting samples were labeled according to the activation temperatures as 600-CL, 800-CL, and 1000-CL, denoting carbonized lignin (CL) treated at 600 °C, 800 °C, and 1000 °C, respectively. Following heat treatment, the samples were thoroughly washed with distilled water to remove any residual KOH, continuing until the wash water reached a neutral pH of approximately 7.

2.2. Nitrogen doping with urea

100 mg of the 800-CL sample was mixed with 500 mg of urea in 3 mL of distilled water. The mixture was sonicated for 10 min to ensure uniform dispersion of urea, a critical step for effective nitrogen doping (the rationale for selecting the 800-CL sample for doping is discussed in the results and discussion section). After sonication, the mixture was transferred to a quartz tube and dried at 80 °C for 12 h in a convection oven to remove any residual moisture, preparing it for the doping process. Subsequent thermal treatment was conducted in an electric tube furnace under an argon atmosphere to prevent oxidation or any undesired reactions. The temperature was systematically increased to the target doping temperatures of 600 °C, 800 °C, or 1000 °C at a rate of 10 °C/min. Upon reaching the designated temperature, it was maintained for 3 h to facilitate thorough nitrogen incorporation into the lignin structure. The resulting samples were designated as 600-NDL, 800-NDL, and 1000-NDL, corresponding to nitrogen-doped lignin (NDL) treated at each specified temperature. This labeling facilitates a clear differentiation between samples treated under varying conditions, allowing for systematic analysis of the doping effects based on the treatment temperature.

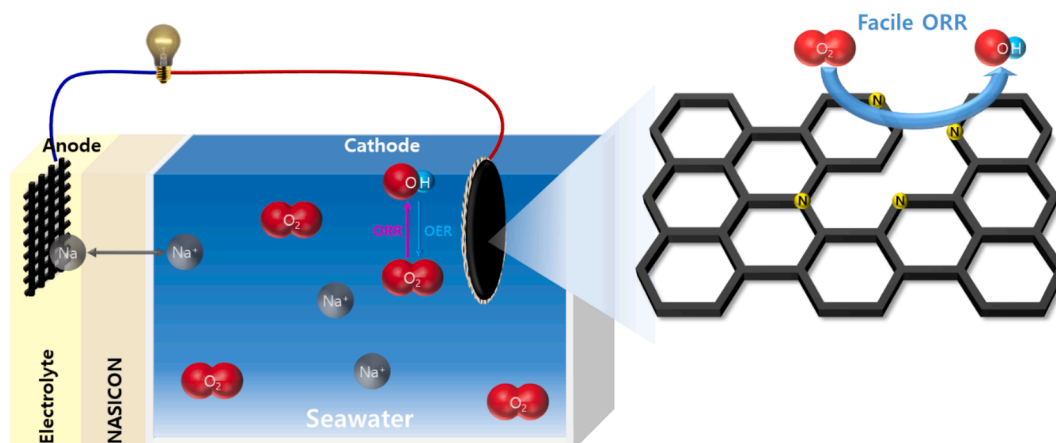


Fig. 1. Graphitic illustration of a seawater battery and a schematic of the catalyst developed in this study.

2.3. Electrochemical measurements of the oxygen reduction reaction

For the electrochemical characterization of the ORR, catalyst ink was prepared as follows: 20 mg of the NDL catalysts were dispersed with 40 μL of Nafion binder (5 wt% in isopropanol; Sigma-Aldrich) in 2 mL of distilled water. This mixture was sonicated for 30 min to ensure a homogenous catalyst ink. Subsequently, 20 μL of this ink was applied onto the surface of a glassy carbon rotating disk electrode (RDE) and dried at 60 $^{\circ}\text{C}$ for 10 min in a convection oven to form a uniform catalyst layer.

The electrochemical measurements were conducted using a three-electrode setup: a glassy carbon electrode as the working electrode, a Hg/HgO electrode as the reference, and a Pt mesh as the counter electrode. To ensure accuracy, the Hg/HgO reference electrode was calibrated against a reversible hydrogen electrode (RHE) through cyclic voltammetry in a two-compartment electrochemical cell, employing the Hg/HgO as the reference and a Pt coil as the working electrode. The experiments were performed in a 0.1 M KOH aqueous solution, starting from 1.2 V down to 0 V versus the RHE, at a scan rate of 5 mV/s. Prior to measurement, the electrolyte was saturated with O_2 for 30 min by purging with O_2 , followed by a constant O_2 flow (50 mL/min) during the scanning process. Linear sweep voltammetry (LSV) was carried out using a multichannel potentiostat (Biologic $\text{\textcircled{C}}$, VSP, France).

2.4. Seawater battery performance test

Catalysts were dip-coated on carbon felt using polyvinylidene fluoride (PVDF) as a binder. Initially, PVDF was dissolved in N-Methyl-2-pyrrolidone (NMP) to create a homogeneous solution. Each catalyst was then dispersed in this solution through 10 min of sonication, ensuring a fine distribution. Subsequently, carbon felt was immersed in the solution and subjected to an additional 5 min of sonication on each side to achieve uniform coating. The catalyst-coated electrodes were dried at 90 $^{\circ}\text{C}$ in a convection oven for three days to ensure thorough solvent evaporation and binder fixation.

Commercial Pt/C (20 % on carbon, Alfa Aesar) and the prepared catalysts were evaluated in a series of tests to assess seawater battery performance, including charge–discharge cycling, rate capability, and peak power evaluation. The charge–discharge cycle test involved alternating 2-hour charge and discharge phases at a current density of 0.25 mA/cm 2 for a total of 200 h, equivalent to 50 cycles. Rate capability was assessed by executing 5 charge–discharge cycles at varying current densities (0.1, 0.2, 0.4, 0.5, 1, and returning to 0.1 mA/cm 2) in sequence. Peak power was determined by discharging the pristine SWB cell to a cut-off voltage of 0.2 V at a current density of 25 mA/cm 2 . These tests were conducted using a WonATech battery testing system (WBCS 3000), ensuring accurate and reproducible measurements.

2.5. Scanning electron microscope (SEM) and energy dispersive X-ray spectroscopy (EDS) analysis

The morphology of the activated samples was meticulously examined using field-emission scanning electron microscope (SEM, model S-4800, Hitachi, Japan) to evaluate the effects of our activation process on the surface structure. Subsequent to nitrogen doping, energy dispersive X-ray spectroscopy (EDS, model SU-7000, Hitachi, Japan) mapping was performed to verify the uniform distribution and presence of nitrogen atoms within the samples, a crucial factor for enhancing their catalytic efficiency.

3. Results and discussion

3.1. Optimization of activation temperature

The carbonization and activation of lignin were conducted according to the procedure mentioned in the Experimental section. SEM analysis revealed that all samples, as depicted in Fig. 2, showcased a rough and porous structure, underscoring the success of the activation process [76,77]. This morphological feature is critical for electrocatalysts, as it potentially enhances the accessible surface area for electrochemical reactions. However, no significant differences in surface morphology were discerned across samples, indicating that the activation temperature did not alter the basic structural characteristics observed via SEM.

To further investigate the activation temperature's impact, we conducted N_2 adsorption–desorption tests, which yielded insights into the surface area of the samples (Fig. 3 and Table S1). Fig. 3a illustrates that the 800-CL sample achieved the highest N_2 adsorption capacity, suggesting a superior surface area of $\sim 2300 \text{ m}^2/\text{g}$. In contrast, the 1000-CL and 600-CL samples demonstrated lower surface areas of $\sim 2030 \text{ m}^2/\text{g}$ and $\sim 1260 \text{ m}^2/\text{g}$, respectively. The increased surface area in the 800-CL sample is indicative of its enhanced potential for catalytic activity, due to a greater availability of active sites for reactions.

The observed differences in surface area can be attributed to the underlying chemical reactions occurring during the activation process. Initially, K_2CO_3 forms at temperatures around 400 $^{\circ}\text{C}$ (Equation (1)). This compound then decomposes into K_2O and CO_2 at temperatures above 700 $^{\circ}\text{C}$ (Equation (2)), with the resultant CO_2 being further reduced to CO (Equation (3)). Additionally, K_2O can react with carbon to produce metallic K and CO. The relatively lower surface area of the 600-CL sample suggests that the decomposition of K_2CO_3 to K_2O and CO_2 was not fully efficient at 600 $^{\circ}\text{C}$. This reaction requires temperatures above 700 $^{\circ}\text{C}$ to proceed effectively, explaining the enhanced porosity and surface area observed in the 800-CL and 1000-CL samples.

Furthermore, the analysis of N_2 adsorption–desorption isotherms

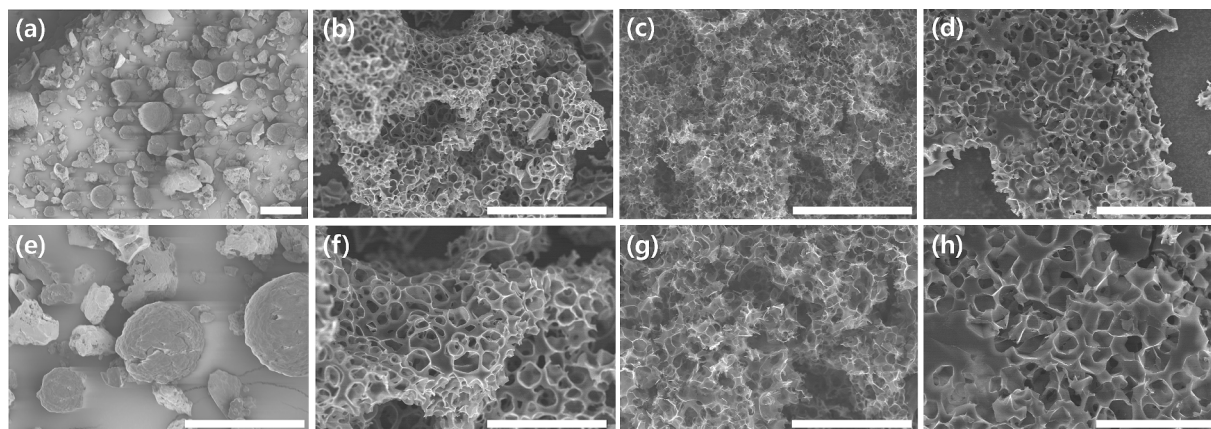


Fig. 2. SEM images of unactivated and activated lignin samples: (a), (e) UCL, (b), (f) 600-CL, (c), (g) 800-CL, and (d), (h) 1000-CL. The scale bars denote 100 μm for (a–d) and 50 μm for (e–h).

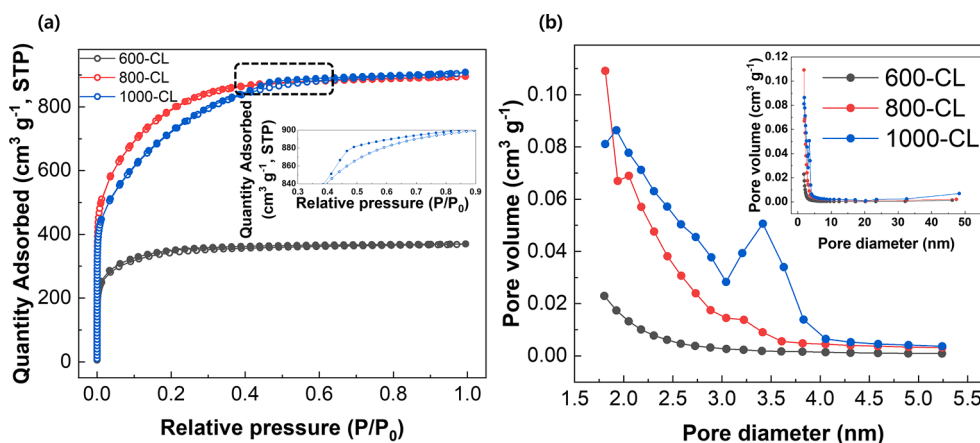


Fig. 3. (a) N_2 adsorption/desorption isotherm curve with an inset showing hysteresis of 1000-CL sample and (b) pore size distribution curve of n -CLs.

(Fig. 3a) revealed distinct pore structures across the different activation temperatures. The 600-CL and 800-CL samples exhibited Type I adsorption isotherms, indicative of a predominantly microporous structure with pore sizes less than 2 nm. This microporous structure is beneficial for electrocatalysis as it may facilitate the accessibility of reactive sites to electrolyte ions. On the other hand, the 1000-CL sample presented a Type IV adsorption isotherm, signifying not only the presence of micropores but also a substantial amount of mesopores (ranging from 2 to 50 nm) [78]. The 800-CL sample exhibits a larger surface area ($2345.5 \text{ m}^2/\text{g}$) compared to the 1000-CL sample ($2032.14 \text{ m}^2/\text{g}$), which contributes to enhanced mass transport and diffusion rates. This is due to excessive activation at 1000°C , which caused the merging of existing pores and resulted in a decrease in surface area. Therefore, 800-CL is considered the most suitable sample for the exploration.

Complementing our understanding of the samples' porosity, the average pore size – determined by the Barrett-Joyner-Halenda (BJH) method and depicted in Fig. 3b – further elucidates the structural nuances influenced by activation temperature. Consistent with their Type I adsorption/desorption isotherms, each sample predominantly exhibited micropore characteristics. Notably, the 1000-CL sample also confirmed the presence of mesopores, with an average size of approximately 3.5

nm, aligning with the observation of a Type IV isotherm curve in Fig. 3a. This presence of mesopores in 1000-CL supports the hypothesis that excessive activation at higher temperatures may lead to reactions that not only create but potentially enlarge pores, through mechanisms suggested in Equations (2) through (5). Such processes could result in pore expansion and eventual merging, accounting for the mesopore presence in 1000-CL.

This observation suggests that while mesopores can enhance mass transport, their formation at the expense of micropores and overall surface area may not be advantageous for ORR performance. Literature supports the notion that micropores and a larger surface area are crucial for enhancing ORR activity [79,80]. Given the largest surface area observed for 800-CL (Table S1) and its rich micropore structure, we identified 800-CL as the optimal sample for further exploration. Consequently, 800-CL was selected for subsequent nitrogen doping experiments, aiming to capitalize on its structural properties to improve electrocatalytic performance.

3.2. Surface analysis of nitrogen-doped lignin (n -NDL)

The doping of activated lignin was conducted according to the

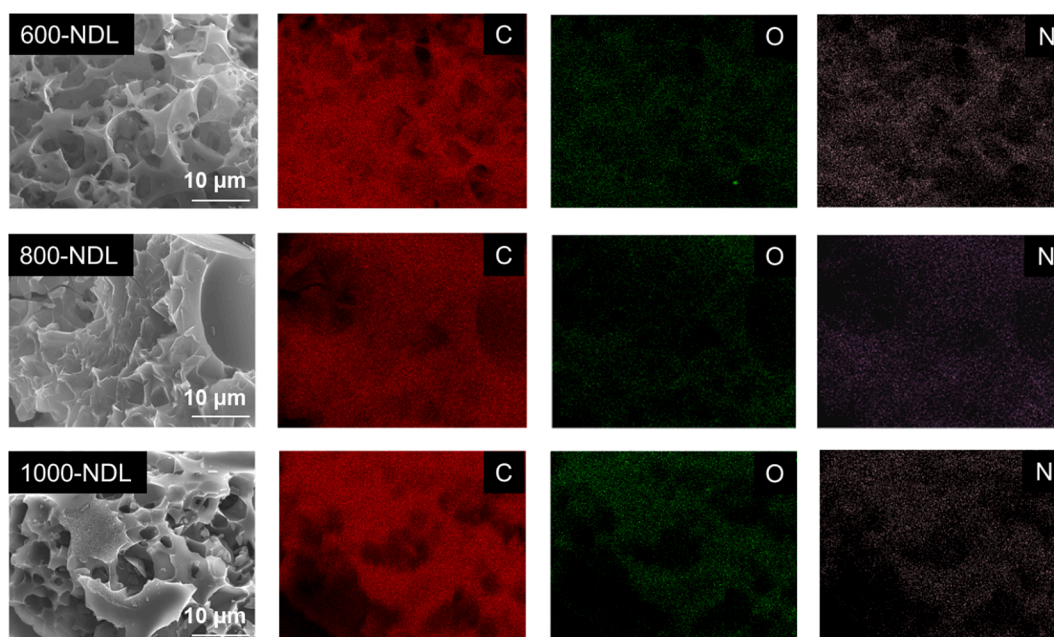


Fig. 4. SEM-EDS elemental mapping images of n -NDL samples after nitrogen doping.

procedure mentioned in the method section. SEM-EDS elemental mapping confirmed the successful integration of nitrogen into the activated lignin across all investigated temperatures (600, 800, and 1000 °C), as depicted in Fig. 4, S1, and S2. The presence of oxygen atoms, detected alongside nitrogen, likely originates from the functional groups inherent to lignin, playing a pivotal role in facilitating nitrogen's solid-state doping [81,82]. High-resolution X-ray photoelectron spectroscopy (XPS) analysis provided deeper insight into the nitrogen-doped structure, identifying four distinct types of nitrogen species [83,84]: pyridinic N, pyrrolic N, graphitic N, and oxidized N-O, as shown in Fig. 5b–d and detailed in Table S2. This analysis revealed a shift in nitrogen configuration with changes in doping temperature, highlighting a decrease in pyrrolic N and an increase in pyridinic N from 600 to 800 °C, with a further shift towards graphitic N at 1000 °C. These findings align with prior studies on N doping in various carbonaceous materials (e.g., graphite oxide [82], graphene oxide [85], lignite, carbazole, and PAN [86]), underscoring the temperature-dependent dynamics of nitrogen incorporation into carbon networks. More specifically, Lin et al. [85] explained that at a relatively low temperature, the nitrogen incorporation occurs mainly at the graphene edges and/or defect sites; while as the annealing temperature rises, the nitrogen atoms start to incorporate into the graphene network, which is consistent with our observation.

Raman spectroscopy further elucidated the material's defect structure, with the I_D/I_G ratio serving as a direct indicator of defects within the carbon lattice (Fig. 6). Prior to doping, the 800-CL sample distinctly displays D and G bands around 1340 /cm and 1590 /cm with an I_D/I_G ratio of 1.00 (Fig. 6a). Post-doping, an increase in this ratio was observed – 1.09 for both 600-NDL and 800-NDL, and 1.03 for 1000-NDL – suggesting an enhanced defect density, particularly in samples doped at lower temperatures (Fig. 6b–d). The elevated I_D/I_G ratios for 600-NDL and 800-NDL can be attributed to the increased content of pyridinic and pyrrolic N, known to introduce defects into the carbon structure [87–90]. Conversely, the relatively lower I_D/I_G ratio for 1000-NDL corresponds with its higher graphitic N content, indicating fewer structural defects. Given the well-documented role of carbon defects in

enhancing ORR activity [17,91,92], the observed increase in I_D/I_G ratios post-doping suggests a potential improvement in the catalytic performance of *n*-NDL. Specifically, the enhanced defect density in 600-NDL and 800-NDL, attributed to pyridinic and pyrrolic nitrogen configurations, may confer superior electrocatalytic properties, underscoring the value of targeted nitrogen doping in optimizing the material for ORR applications.

3.3. Evaluation of catalytic activity

Evaluation of the catalytic activity in 0.1 M KOH through Linear Sweep Voltammetry (LSV) data identified three critical parameters: onset potential (E_{onset}), half-wave potential ($E_{1/2}$), and limiting current density. E_{onset} marks the electrochemical reaction's initiation, while $E_{1/2}$ represents a holistic measure of mass transfer and surface reaction dynamics, serving as a pivotal indicator of ORR activity [93]. The limiting current density indicates the extent of the electrochemical reaction.

In the initial step of the electrochemical reaction, Lewis base sites are created by pyridinic N. O₂ molecules are first adsorbed onto carbon atoms adjacent to the pyridinic N and then protonated. These active sites generate minor currents, resulting in a non-flat baseline [94]. Among the tested samples, 800-NDL demonstrated the most favorable electrochemical performance, as evidenced in Fig. 7 and S3. with the highest E_{onset} and $E_{1/2}$ values of 0.84 V and 0.75 V, respectively. This outperforms the 1000-NDL, which shows slightly lower values (0.83 V and 0.74 V) and has a lower pyridinic N content compared to the 800-NDL (Fig. 5c and d). Both the 800-NDL and 1000-NDL significantly exceed the performance of 600-NDL (E_{onset} and $E_{1/2}$ at 0.81 V and 0.72 V). The observed limiting current densities – 6.56 mA/cm² for 800-NDL, 6.44 mA/cm² for 1000-NDL, and 5.92 mA/cm² for 600-NDL – further corroborate these findings, underlining a direct link between the nitrogen-doped structure and catalytic efficiency. The difference in electronegativity between nitrogen and carbon causes C–N bonds of pyridinic N to be consistently polarized. This results in a slight negative charge on the nitrogen atoms and a corresponding slight positive charge

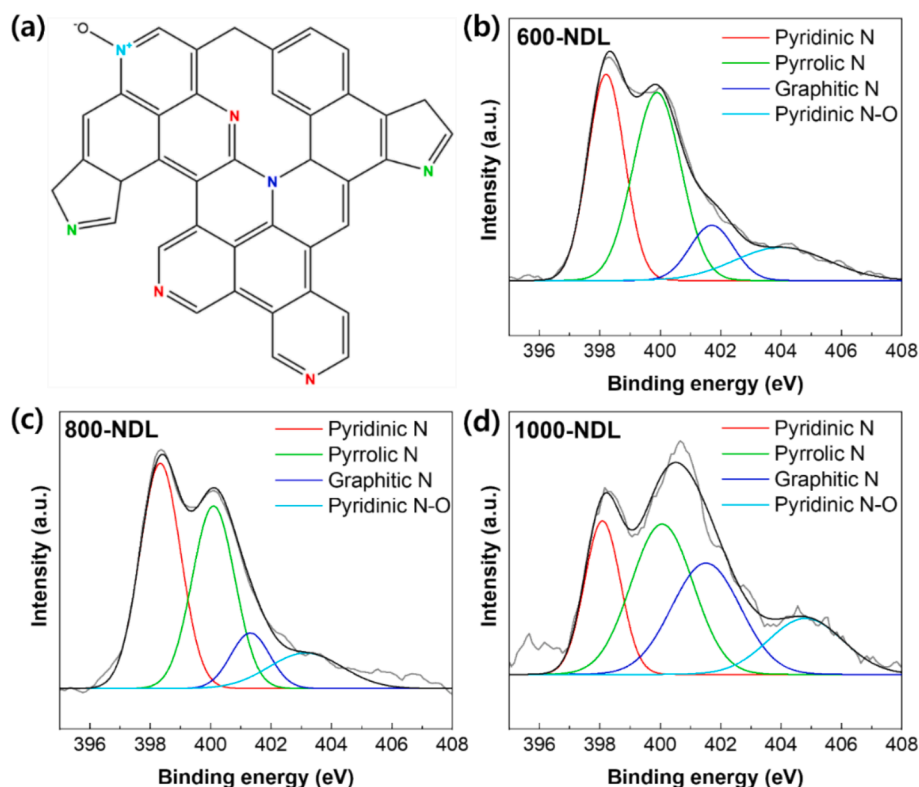


Fig. 5. (a) Structure of nitrogen-doped lignin (NDL), and high resolution XPS spectra of (b) 600-NDL, (c) 800-NDL, and (d) 1000-NDL.

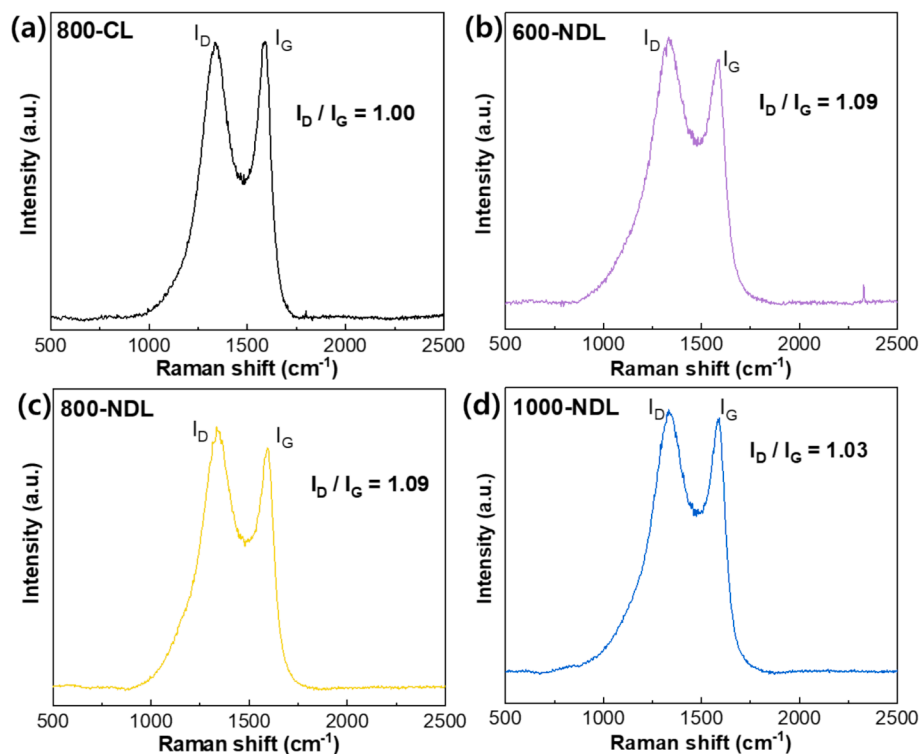


Fig. 6. (a) Raman spectra before doping (800-CL), (b-d) after doping. (b) 600-NDL, (c) 800-NDL, (d) 1000-NDL.

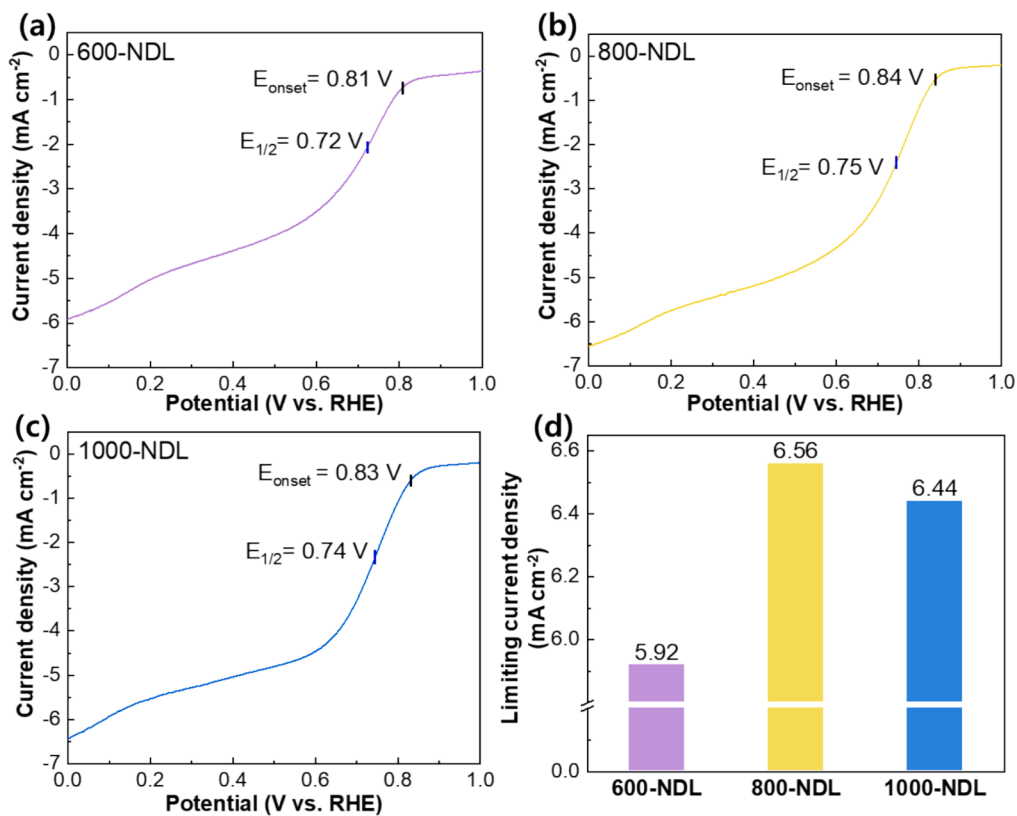


Fig. 7. Evaluation of catalytic activity in different samples using 0.1 M KOH solution. LSV curves of (a) 600-NDL, (b) 800-NDL and (c) 1000-NDL, and (d) limiting current density of the samples.

on the adjacent carbon atoms [95]. This charge distribution is crucial for catalytic efficiency and directly influences the observed limiting current density by facilitating enhanced electron transfer rates and reducing mass transport limitations.

Many studies have examined the beneficial effects of nitrogen doping on ORR [42,79,96–98], but the most effective nitrogen configuration for enhancing ORR activity is ongoing debate [99–104]. Our findings suggest a pronounced effect of pyridinic N on catalytic performance, with 800-NDL, which boasts the highest pyridinic N content, showing superior activity. The reasonably high activity of 1000-NDL, enriched in graphitic N, also underscores the significant role of this nitrogen configuration in ORR, indicating that both types of nitrogen species contribute meaningfully to the catalytic process.

3.4. Seawater battery (SWB) performance

In our evaluation of SWB performance, the doped catalysts were applied to the cathode, revealing compelling results, particularly for 800-NDL. First, the charge/discharge cycle test was conducted for 200 h (~50 cycles) and all samples were stable without cell failure (Fig. 8a). Notably, 800-NDL demonstrated the smallest voltage gap during these cycles (~0.71 V), consistent with its superior performance observed in LSV tests and closely mirroring the performance of the benchmark Pt/C catalyst (~0.74 V) as shown in Fig. 8b. Additionally, This value is comparable to those of Ir/C (~0.73 V) [17] and MnO_2 (~0.73 V) [105] for catalysts. These results indicate a significant reduction in overpotential with 800-NDL, underscoring its efficiency.

Further evaluation through rate capability tests at varying current

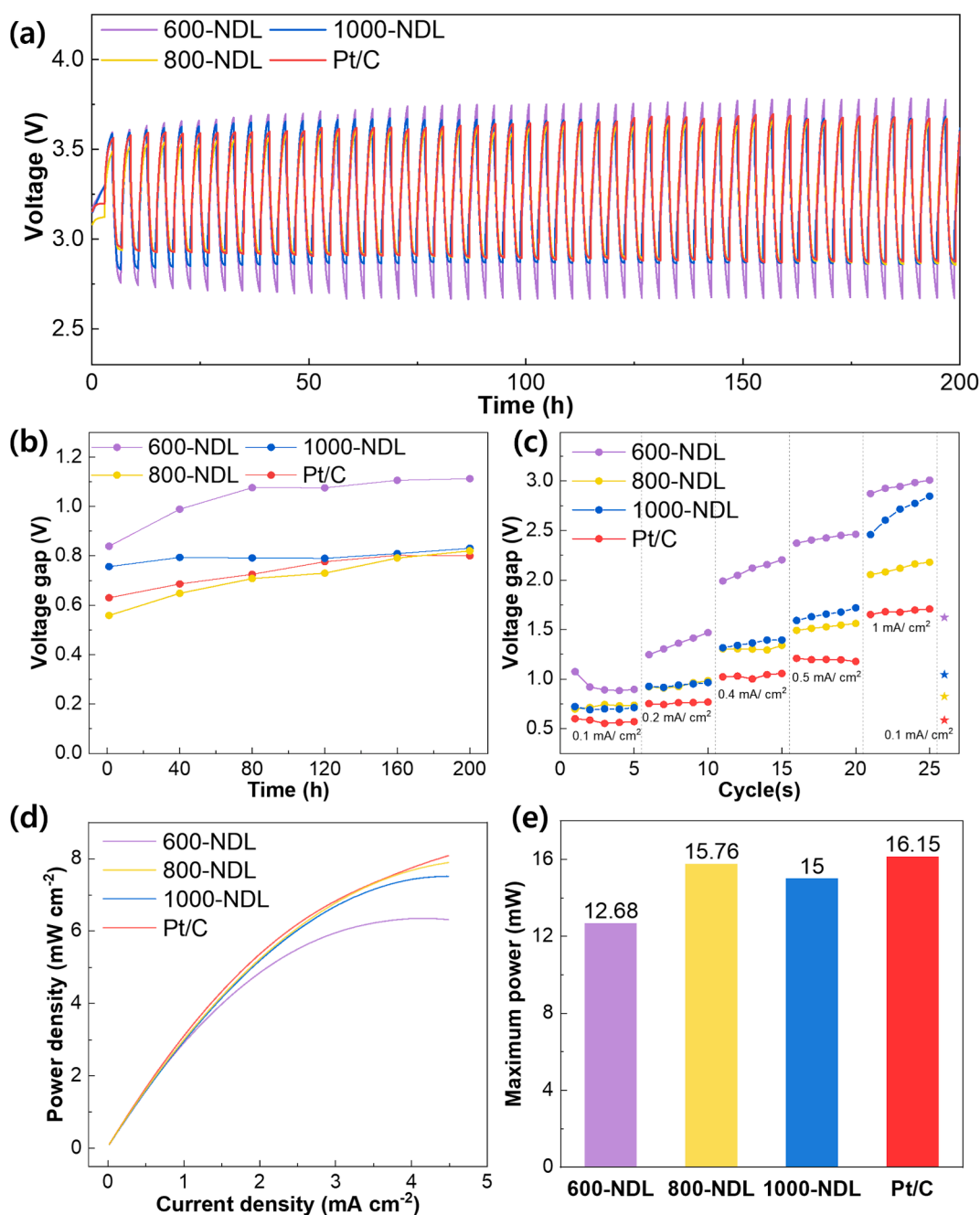


Fig. 8. Seawater battery performance test of the samples showing (a) charge–discharge cycle test, (b) charge–discharge voltage gap from (a), (c) voltage gap of rate capability test, (d) discharge power curve of the samples, (e) maximum power from (d).

densities revealed the robust performance of 800-NDL (Fig. 8c and S4). While samples 1000-NDL and 600-NDL exhibited high voltage gaps exceeding 2.5 V at the highest current density of 1 mA/cm², indicating suboptimal performance, 800-NDL maintained a consistently lower voltage gap across all current densities. Crucially, it was the only sample to fully recover its initial voltage gap following the high current density test, showcasing its exceptional resilience and performance consistency.

The power curves and maximum power outputs of the NDL and Pt/C samples further emphasize the potential of 800-NDL. With a maximum power of 15.76 mW, 800-NDL closely approaches the performance of Pt/C, which exhibits a maximum power of 16.15 mW. The 1000-NDL and 600-NDL samples, however, lag behind, with lower maximum power outputs of 15 mW and 12.68 mW, respectively (Fig. 8d and e). This indicates that the enhanced electrochemical performance is attributed to an increased number of active sites resulting from nitrogen doping. Nitrogen doping modifies the electronic properties of the carbon material by creating active sites for oxygen adsorption and reduction. Hence, it improves the electrical conductivity and structural stability of the carbon material and further enhances ORR performances [57,104].

These findings compellingly demonstrate that the SWB incorporating 800-NDL competes favorably with the conventional Pt/C catalyst in terms of voltage gap (0.71 V vs. 0.74 V) and maximum power (15.76 mW vs. 16.15 mW). Given the significant cost advantage of 800-NDL (which is discussed in next section) over Pt/C, our study highlights the potential of 800-NDL as a viable and economically feasible ORR catalyst alternative. This breakthrough opens avenues for further optimization and exploration of nitrogen-doped catalysts in seawater batteries and beyond, promising a more sustainable and cost-effective future for energy storage solutions.

3.5. Price competitiveness of 800-NDL

As of March 2024, 1 kg of Pt/C (Sigma-Aldrich) is priced at €16,998. In contrast, the cost to produce 1 kg of 800-NDL, including raw material and energy expenses, is €5,144, as detailed in the calculations provided in supplementary material. This price represents only 30 % of the cost of an equivalent quantity of Pt/C. It is important to note that these calculations are based on the use of reagent-grade materials (for both lignin and urea) in lab-scale production (using a small furnace operated for approximately ~7,000 h to produce 1 kg of 800-NDL). The cost of producing 800-NDL could be significantly reduced, indicating an even greater potential for cost savings through the utilization of lignin and urea derived from industrial and wastewater sources, and by scaling up the production process.

4. Conclusion

In this research, we successfully synthesized an electrocatalyst for seawater batteries, leveraging lignin from biomass and urea from bio-waste, highlighting a novel, sustainable approach to catalyst design. The activation of lignin at 800 °C yielded a material (800-CL) with an exceptional surface area of ~2345.5 m²/g, underscoring the effectiveness of our carbonization and activation process. Subsequent nitrogen doping of 800-CL at varying temperatures revealed distinct structural variations, with the sample doped at 800 °C (800-NDL) demonstrating superior catalytic activity. This can be attributed to its enriched pyridinic nitrogen content, emphasizing the critical role of this nitrogen configuration in enhancing ORR performance. Notably, a seawater battery incorporating 800-NDL achieved performance on par with those using the traditional Pt/C catalyst, marking a significant advancement in the development of cost-effective and sustainable electrocatalysts. Furthermore, the cost analysis revealed that producing 1 kg of 800-NDL could be achieved at approximately ~30 % of the cost of an equivalent amount of Pt/C. This substantial cost reduction, even when utilizing reagent-grade materials, suggests that utilizing industrial by-products as sources for lignin and urea could further enhance the economic viability

of this approach.

The findings from this study not only reinforce the potential of biomass-derived materials in electrocatalysis but also open new pathways for the application of this sustainable catalyst in a broader range of energy systems, including alkaline fuel cells and metal-air batteries. Moving forward, the exploration of such cost-effective and environmentally benign materials promises to accelerate the transition towards more sustainable energy storage and conversion technologies.

Author contributions

Ji Hwan Hong and Inwoo Song contributed equally to this work. The manuscript was written through contributions of all authors. All authors have given approval to the final version of the manuscript.

CRediT authorship contribution statement

Ji Hwan Hong: Writing – review & editing, Writing – original draft, Validation, Methodology, Investigation, Formal analysis, Data curation. **Inwoo Song:** Writing – review & editing, Writing – original draft, Validation, Investigation, Formal analysis, Data curation, Conceptualization. **Yoonjong Cho:** Methodology, Investigation. **Jinhoon Lee:** Methodology, Investigation. **Jee Ho Ha:** Data curation, Formal analysis. **Myung-Jin Baek:** Writing – review & editing, Validation, Supervision. **Seok Ju Kang:** Supervision. **Dong Woog Lee:** Writing – review & editing, Validation, Supervision, Resources, Project administration, Investigation, Funding acquisition.

Declaration of competing interest

The authors declare that they have no known competing financial interests or personal relationships that could have appeared to influence the work reported in this paper.

Acknowledgments

This research was supported by the Basic Science Research Program (NRF-2023R1A2C2004762) and the Nano & Material Technology Development Program (RS-2024-00408845) through the National Research Foundation of Korea (NRF) grant funded by the Ministry of Science and ICT, South Korea.

Data availability

Data will be made available on request.

References

- [1] J.-Y. Zhang, Y. Yan, B. Mei, R. Qi, T. He, Z. Wang, W. Fang, S. Zaman, Y. Su, S. Ding, Local spin-state tuning of cobalt–iron selenide nanoframes for the boosted oxygen evolution, *Energy Environ. Sci.* 14 (1) (2021) 365–373.
- [2] G. Martin, L. Rentsch, M. Höck, M. Bertau, Lithium market research–global supply, future demand and price development, *Energy Storage Mater.* 6 (2017) 171–179.
- [3] Y. Shi, Y. Feng, Q. Zhang, J. Shuai, J. Niu, Does China's new energy vehicles supply chain stock market have risk spillovers? Evidence from Raw Material Price Effect on Lithium Batteries, *Energy* 262 (2023) 125420.
- [4] X. Sun, M. Ouyang, H. Hao, Surging lithium price will not impede the electric vehicle boom, *Joule* 6 (8) (2022) 1738–1742.
- [5] J. Song, W. Yan, H. Cao, Q. Song, H. Ding, Z. Lv, Y. Zhang, Z. Sun, Material flow analysis on critical raw materials of lithium-ion batteries in China, *J. Cleaner Prod.* 215 (2019) 570–581.
- [6] V. Flexer, C.F. Baspineiro, C.I. Galli, Lithium recovery from brines: A vital raw material for green energies with a potential environmental impact in its mining and processing, *Sci. Total Environ.* 639 (2018) 1188–1204.
- [7] T. Zheng, P. Hu, Z. Wang, T. Guo, 2D Amorphous Iron Selenide Sulfide Nanosheets for Stable and Rapid Sodium-Ion Storage, *Adv. Mater.* 35 (48) (2023) 2306577.
- [8] M.L. Vera, W.R. Torres, C.I. Galli, A. Chagnes, V. Flexer, Environmental impact of direct lithium extraction from brines, *Nat. Rev. Earth Environ.* 4 (3) (2023) 149–165.

- [9] A.C. Schomberg, S. Bringezu, M. Flörke, Extended life cycle assessment reveals the spatially-explicit water scarcity footprint of a lithium-ion battery storage, *Commun. Earth Environ* 2 (1) (2021) 11.
- [10] R.B. Kaunda, Potential environmental impacts of lithium mining, *J.E.R.L.* 38 (3) (2020) 237–244.
- [11] T.T.N. Tran, T.A. Le, N.T.T. Dinh, N.D. Hai, T.-K. Truong, J. Yu, L. Peng, C. C. Nguyen, N.Q. Tran, Crystalline Ru-Decorated MOF-Derived Amorphous CoMo-LDH Nanosheet Arrays as Bifunctional Catalysts for Overall Natural Seawater Electrolysis, *ACS Appl. Mater. Interfaces* 16 (40) (2024) 53675–53687.
- [12] P. He, T. Zhang, J. Jiang, H. Zhou, Lithium–air batteries with hybrid electrolytes, *J. Phys. Chem. Lett.* 7 (7) (2016) 1267–1280.
- [13] S. Senthilkumar, W. Go, J. Han, L.P.T. Thuy, K. Kishor, Y. Kim, Y. Kim, Emergence of rechargeable seawater batteries, *J. Mater. Chem. A* 7 (40) (2019) 22803–22825.
- [14] J.K. Kim, E. Lee, H. Kim, C. Johnson, J. Cho, Y. Kim, Rechargeable seawater battery and its electrochemical mechanism, *ChemElectroChem* 2 (3) (2015) 328–332.
- [15] N. Kim, S. Jeong, W. Go, Y. Kim, A Na⁺ ion-selective desalination system utilizing a NASICON ceramic membrane, *Water Res.* 215 (2022) 118250.
- [16] P. Sharma, J. Han, J. Park, D.Y. Kim, J. Lee, D. Oh, N. Kim, D.-H. Seo, Y. Kim, S. J. Kang, Alkali-metal-mediated reversible chemical hydrogen storage using seawater, *JACS Au* 1 (12) (2021) 2339–2348.
- [17] S. Senthilkumar, S.O. Park, J. Kim, S.M. Hwang, S.K. Kwak, Y. Kim, Seawater battery performance enhancement enabled by a defect/edge-rich, oxygen self-doped porous carbon electrocatalyst, *J. Mater. Chem. A* 5 (27) (2017) 14174–14181.
- [18] J. Park, J.-S. Park, S. Senthilkumar, Y. Kim, Hybridization of cathode electrochemistry in a rechargeable seawater battery: Toward performance enhancement, *J. Power Sources* 450 (2020) 227600.
- [19] Y. Cho, J. Park, W.G. Lee, J. Park, K. Shin, I. Song, G. Lee, J. Cho, S.J. Kang, Y. Kim, Prevention of Carbon Corrosion by TiC Formation on Ti Current Collector in Seawater Batteries, *Adv. Funct. Mater.* 2213853 (2023).
- [20] J. Li, J. Zhao, Z. Lai, Y. Zhang, Y. Wang, R. Jia, H. Wang, Z. Yin, J. Zhang, X. Zheng, Efficient and stable neutral seawater splitting achieved via strong-proton-adsorption in Pd-O-Co collaborative coordination, *Chem. Eng. J.* 492 (2024) 152226.
- [21] N.Q. Tran, N.H. Vu, J. Yu, K.V.P. Nguyen, T.T.N. Tran, T.-K. Truong, L. Peng, T. A. Le, Y. Kawazoe, Generating highly active oxide-phosphide heterostructure through interfacial engineering to break the energy scaling relation toward urea-assisted natural seawater electrolysis, *J. Energy Chem.* 97 (2024) 687–699.
- [22] Y. Wang, X. Li, M. Zhang, Y. Zhou, D. Rao, C. Zhong, J. Zhang, X. Han, W. Hu, Y. Zhang, Lattice-strain engineering of homogeneous NiSeO₅SeO₅ 5 core-shell nanostructure as a highly efficient and robust electrocatalyst for overall water splitting, *Adv. Mater.* 32 (40) (2020) 2000231.
- [23] S. Brankovic, J. Wang, R. Adžić, Pt submonolayers on Ru nanoparticles: a novel low Pt loading, high CO tolerance fuel cell electrocatalyst, *Electrochem. Solid-State Lett.* 4 (12) (2001) A217.
- [24] F.-D. Kong, J. Liu, A.-X. Ling, Z.-Q. Xu, M.-J. Shi, Q.-S. Kong, H.-Y. Wang, Overlapping structure of platinum-iridium oxide layers and its electrocatalytic behavior on bifunctional oxygen electrode, *Catal. Commun.* 90 (2017) 19–22.
- [25] F. Zhao, B. Wen, W. Niu, Z. Chen, C. Yan, A. Selloni, C.G. Tully, X. Yang, B. E. Koel, Increasing iridium oxide activity for the oxygen evolution reaction with hafnium modification, *J. Am. Chem. Soc.* 143 (38) (2021) 15616–15623.
- [26] Y. Li, L. Zhou, S. Guo, Noble metal-free electrocatalytic materials for water splitting in alkaline electrolyte, *EnergyChem* 3 (2) (2021) 100053.
- [27] X. Han, X. Wu, Y. Deng, J. Liu, J. Lu, C. Zhong, W. Hu, Ultrafine Pt nanoparticle-decorated pyrite-type CoS₂ nanosheet arrays coated on carbon cloth as a bifunctional electrode for overall water splitting, *Adv. Energy Mater.* 8 (24) (2018) 1800935.
- [28] H. Xu, H. Shang, C. Wang, Y. Du, Surface and interface engineering of noble-metal-free electrocatalysts for efficient overall water splitting, *Coord. Chem. Rev.* 418 (2020) 213374.
- [29] K. Dong, Y. Lei, H. Zhao, J. Liang, P. Ding, Q. Liu, Z. Xu, S. Lu, Q. Li, X. Sun, Noble-metal-free electrocatalysts toward H₂O₂ production, *J. Mater. Chem. A* 8 (44) (2020) 23123–23141.
- [30] S. Shit, S. Bolar, N.C. Murmu, T. Kuila, An account of the strategies to enhance the water splitting efficiency of noble-metal-free electrocatalysts, *J. Energy Chem.* 59 (2021) 160–190.
- [31] W. Wu, S. Yang, H. Qian, L. Zhang, L. Peng, L. Li, B. Liu, Z. Wei, Interface engineering of advanced electrocatalysts toward alkaline hydrogen evolution reactions, *Chin. J. Catal.* 66 (2024) 1–19.
- [32] Y. Wang, X. Li, M. Zhang, J. Zhang, Z. Chen, X. Zheng, Z. Tian, N. Zhao, X. Han, K. Zaghbi, Highly active and durable single-atom tungsten-doped NiSeO₅SeO₅ 5 nanosheet@NiSeO₅SeO₅ 5 nanorod heterostructures for water splitting, *Adv. Mater.* 34(13) (2022) 2107053.
- [33] Y. Wang, X. Li, Z. Huang, H. Wang, Z. Chen, J. Zhang, X. Zheng, Y. Deng, W. Hu, A.M.-d. NiS₅SeO₅ 5 nanosheets@ crystalline NiSeO₅SeO₅ 5 nanorods for high current-density electrocatalytic water splitting in neutral media, *Angew. Chem. Int. Ed* 62 (2023) e202215256.
- [34] F. Qian, L. Peng, D. Cao, W. Jiang, C. Hu, J. Huang, X. Zhang, J. Luo, S. Chen, X. Wu, Asymmetric active sites originate from high-entropy metal selenides by joule heating to boost electrocatalytic water oxidation, *Joule* 8 (8) (2024) 2342–2356.
- [35] Y. Wang, M. Jiao, W. Song, Z. Wu, Doped fullerene as a metal-free electrocatalyst for oxygen reduction reaction: A first-principles study, *Carbon* 114 (2017) 393–401.
- [36] X. Lu, W.-L. Yim, B.H. Suryanto, C. Zhao, Electrocatalytic oxygen evolution at surface-oxidized multiwall carbon nanotubes, *J. Am. Chem. Soc.* 137 (8) (2015) 2901–2907.
- [37] M. Li, L. Zhang, Q. Xu, J. Niu, Z. Xia, N-doped graphene as catalysts for oxygen reduction and oxygen evolution reactions: Theoretical considerations, *J. Catal.* 314 (2014) 66–72.
- [38] C.K. Chua, M. Pumera, Monothiolation and reduction of graphene oxide via one-pot synthesis: hybrid catalyst for oxygen reduction, *ACS Nano* 9 (4) (2015) 4193–4199.
- [39] A. Abdolmaleki, S. Mallakpour, M. Mahmoudian, S. Kamali, M. Zhiani, B. Rezaei, A.R.T. Jahromi, Functionalization of Graphite with the Diels–Alder Reaction to Fabricate Metal-Free Electrocatalysts for Highly Efficient Hydrogen Evolution Reaction, *ChemistrySelect* 3 (46) (2018) 13070–13075.
- [40] Y.M. Manawi, A. Ihsanullah, T. Samara, M.A.A. Al-Ansari, A review of carbon nanomaterials' synthesis via the chemical vapor deposition (CVD) method, *Materials* 11 (5) (2018) 822.
- [41] M. Hassan, V.G. Gomes, Coal derived carbon nanomaterials—Recent advances in synthesis and applications, *Appl. Mater. Today* 12 (2018) 342–358.
- [42] C. Murugesan, B. Senthilkumar, P. Barpanda, Biowaste-derived highly porous N-doped carbon as a low-cost bifunctional electrocatalyst for hybrid sodium–air batteries, *ACS Sustainable Chem. Eng.* 10 (28) (2022) 9077–9086.
- [43] Y. Fang, H. Wang, H. Yu, F. Peng, From chicken feather to nitrogen and sulfur co-doped large surface bio-carbon floccs: an efficient electrocatalyst for oxygen reduction reaction, *Electrochim. Acta* 213 (2016) 273–282.
- [44] Z.-Z. Chang, B.-J. Yu, C.-Y. Wang, Lignin-derived hierarchical porous carbon for high-performance supercapacitors, *J. Solid State Electrochem.* 20 (2016) 1405–1412.
- [45] K. Mikami, M. Funaoka, Polymer Structure of Lignophenol II—Comparison of Molecular Morphology of Lignophenol and Conventional Lignins—, *Polym. J.* 38 (6) (2006) 592–596.
- [46] C.G. Yoo, A.J. Ragauskas, Opportunities and challenges of lignin utilization, From Processing to Applications, *Lignin Utilization Strategies*, 2021, pp. 1–12.
- [47] H. Wang, Y. Pu, A. Ragauskas, B. Yang, From lignin to valuable products—strategies, challenges, and prospects, *Bioresour. Technol.* 271 (2019) 449–461.
- [48] S.-H. Li, S. Liu, J.C. Colmenares, Y.-J. Xu, A sustainable approach for lignin valorization by heterogeneous photocatalysis, *Green Chem.* 18 (3) (2016) 594–607.
- [49] E. Rosini, F. Molinari, D. Miani, L. Pollegioni, Lignin valorization: production of high value-added compounds by engineered microorganisms, *Catalysts* 13 (3) (2023) 555.
- [50] R. Font, M. Esperanza, A.N. Garcia, Toxic by-products from the combustion of Kraft lignin, *Chemosphere* 52 (6) (2003) 1047–1058.
- [51] L. Dessbesell, M. Paleologou, M. Leitch, R. Pulkki, C.C. Xu, Global lignin supply overview and kraft lignin potential as an alternative for petroleum-based polymers, *Renewable and Sustainable Energy Reviews* 123 (2020) 109768.
- [52] M. Zirbes, T. Graßl, R. Neuber, S.R. Waldvogel, Peroxidocarbonate as a Green Oxidizer for the Selective Degradation of Kraft Lignin into Vanillin, *Angew. Chem. Int. Ed.* 62 (14) (2023) e202219217.
- [53] M. Shakhmari, S. Emmanuel, D.B. Hodge, M. Nejad, Lignin-Glyoxal: A fully biobased formaldehyde-free wood adhesive for interior engineered wood products, *ACS Sustainable Chem. Eng.* 10 (11) (2022) 3430–3441.
- [54] R. Liu, L. Dai, C. Xu, K. Wang, C. Zheng, C. Si, Lignin-based micro-and nanomaterials and their composites in biomedical applications, *ChemSusChem* 13 (17) (2020) 4266–4283.
- [55] M.A. Jedrzejczyk, J. Engelhardt, M.R. Djokic, V. Bliznuk, K.M. Van Geem, A. Verberckmoes, J. De Clercq, K.V. Bernaerts, Development of lignin-based mesoporous carbons for the adsorption of humic acid, *ACS Omega* 6 (23) (2021) 15222–15235.
- [56] F. Torres-Canas, A. Bentaleb, M. Föllmer, J. Roman, W. Neri, I. Ly, A. Derré, P. Poulin, Improved structure and highly conductive lignin-carbon fibers through graphene oxide liquid crystal, *Carbon* 163 (2020) 120–127.
- [57] Y. Xi, D. Yang, W. Liu, Y. Qin, X. Qiu, Preparation of porous lignin-derived carbon/carbon nanotube composites by hydrophobic self-assembly and carbonization to enhance lithium storage capacity, *Electrochim. Acta* 303 (2019) 1–8.
- [58] M. Cao, Q. Wang, W. Cheng, S. Huan, Y. Hu, Z. Niu, G. Han, H. Cheng, G. Wang, A novel strategy combining electrospraying and one-step carbonization for the preparation of ultralight honeycomb-like multilayered carbon from biomass-derived lignin, *Carbon* 179 (2021) 68–79.
- [59] J. Gu, S. Magagula, J. Zhao, Z. Chen, Boosting ORR/OER activity of graphdiyne by simple heteroatom doping, *Small Methods* 3 (9) (2019) 1800550.
- [60] J. Quílez-Bermejo, E. Morallón, D. Cazorla-Amorós, Metal-free heteroatom-doped carbon-based catalysts for ORR: A critical assessment about the role of heteroatoms, *Carbon* 165 (2020) 434–454.
- [61] X. Feng, Y. Bai, M. Liu, Y. Li, H. Yang, X. Wang, C. Wu, Untangling the respective effects of heteroatom-doped carbon materials in batteries, supercapacitors and the ORR to design high performance materials, *Energy Environ. Sci.* 14 (4) (2021) 2036–2089.
- [62] K. Gong, F. Du, Z. Xia, M. Durstock, L. Dai, Nitrogen-doped carbon nanotube arrays with high electrocatalytic activity for oxygen reduction, *Science* 323 (5915) (2009) 760–764.
- [63] T. Xing, Y. Zheng, L.H. Li, B.C. Cowie, D. Gunzelmann, S.Z. Qiao, S. Huang, Y. Chen, Observation of active sites for oxygen reduction reaction on nitrogen-doped multilayer graphene, *ACS Nano* 8 (7) (2014) 6856–6862.

- [64] J.-C. Li, X. Qin, P.-X. Hou, M. Cheng, C. Shi, C. Liu, H.-M. Cheng, M. Shao, Identification of active sites in nitrogen and sulfur co-doped carbon-based oxygen reduction catalysts, *Carbon* 147 (2019) 303–311.
- [65] C. Bie, H. Yu, B. Cheng, W. Ho, J. Fan, J. Yu, Design, fabrication, and mechanism of nitrogen-doped graphene-based photocatalyst, *Adv. Mater.* 33 (9) (2021) 2003521.
- [66] F. Fu, D. Yang, Y. Fan, X. Qiu, J. Huang, Z. Li, W. Zhang, Nitrogen-rich accordion-like lignin porous carbon via confined self-assembly template and in-situ mild activation strategy for high-performance supercapacitors, *J. Colloid Interface Sci.* 628 (2022) 90–99.
- [67] J. Tan, H. Chen, Y. Gao, H. Li, Nitrogen-doped porous carbon derived from citric acid and urea with outstanding supercapacitance performance, *Electrochim. Acta* 178 (2015) 144–152.
- [68] E. Urbanićzyk, M. Sowa, W. Simka, Urea removal from aqueous solutions—a review, *J. Appl. Electrochem.* 46 (2016) 1011–1029.
- [69] I.H.R. Abbasi, F. Abbasi, M.E. Abd El-Hack, M.A. Abdel-Latif, R.N. Soomro, K. Hayat, M.A. Mohamed, B.M. Bodinga, J. Yao, Y. Cao, Critical analysis of excessive utilization of crude protein in ruminants ration: impact on environmental ecosystem and opportunities of supplementation of limiting amino acids—a review, *Environ. Sci. Pollut. Res.* 25 (2018) 181–190.
- [70] B.K. Boggs, R.L. King, G.G. Botte, Urea electrolysis: direct hydrogen production from urine, *Chem. Commun.* 32 (2009) 4859–4861.
- [71] A. Zaher, N. Shehata, Recent advances and challenges in management of urea wastewater: A mini review, *IOP Conference Series: Materials Science and Engineering*, IOP Publishing (2021) 012021.
- [72] Y. Wu, H. Wang, J. Ren, X. Xu, X. Wang, R. Wang, Electrocatalyst based on Ni₂P nanoparticles and NiCoP nanosheets for efficient hydrogen evolution from urea wastewater, *J. Colloid Interface Sci.* 608 (2022) 2932–2941.
- [73] S. Nangan, Y. Ding, A.Z. Alhakemy, Y. Liu, Z. Wen, Hybrid alkali-acid urea-nitrate fuel cell for degrading nitrogen-rich wastewater, *Appl. Catal., B* 286 (2021) 119892.
- [74] W. Yan, D. Wang, G.G. Botte, Electrochemical decomposition of urea with Ni-based catalysts, *Appl. Catal., B* 127 (2012) 221–226.
- [75] W. Zhang, J. Yin, C. Wang, L. Zhao, W. Jian, K. Lu, H. Lin, X. Qiu, H.N. Alshareef, Lignin derived porous carbons: synthesis methods and supercapacitor applications, *Small Methods* 5 (11) (2021) 2100896.
- [76] V. Efeovbokhan, E. Alagbe, B. Odika, R. Babalola, T. Oladimeji, O. Abatan, E. Yusuf, Preparation and characterization of activated carbon from plantain peel and coconut shell using biological activators, *Journal of Physics: Conference Series*, IOP Publishing (2019) 032035.
- [77] A. Alabadi, H.A. Abbood, Q. Li, N. Jing, B. Tan, Imine-linked polymer based nitrogen-doped porous activated carbon for efficient and selective CO₂ capture, *Sci. Rep.* 6 (1) (2016) 38614.
- [78] Z.a. AlOthman, A review: fundamental aspects of silicate mesoporous materials, *Materials* 5 (12) (2012) 2874–2902.
- [79] B. Xie, Y. Zhang, R. Zhang, Pure nitrogen-doped graphene aerogel with rich micropores yields high ORR performance, *Mater. Sci. Eng. B* 242 (2019) 1–5.
- [80] G. Leofanti, M. Padovan, G. Tozzola, B. Venturini, Surface area and pore texture of catalysts, *Catal. Today* 41 (1–3) (1998) 207–219.
- [81] Z. Huang, Z. Liao, W. Yang, H. Zhou, C. Fu, Y. Gong, L. Chen, Y. Kuang, Different types of nitrogen species in nitrogen-doped carbon material: The formation mechanism and catalytic role on oxygen reduction reaction, *Electrochim. Acta* 245 (2017) 957–966.
- [82] Z. Mou, X. Chen, Y. Du, X. Wang, P. Yang, S. Wang, Forming mechanism of nitrogen doped graphene prepared by thermal solid-state reaction of graphite oxide and urea, *Appl. Surf. Sci.* 258 (5) (2011) 1704–1710.
- [83] Z. Zhu, Z. Li, J. Wang, R. Li, H. Chen, Y. Li, J.S. Chen, R. Wu, Z. Wei, Improving Ni₂N and pyridinic N active sites with space-confined pyrolysis for effective CO₂ electroreduction, *eScience* 2 (4) (2022) 445–452.
- [84] L. Vanyorek, A. Prekora, V. Hajdu, G. Muranszky, B. Fiser, E. Sikora, F. Kristaly, B. Viskolcz, Ultrasonic cavitation assisted deposition of catalytically active metals on nitrogen-doped and non-doped carbon nanotubes—A comparative study, *J. Mater. Res. Technol.* 9 (3) (2020) 4283–4291.
- [85] Z. Lin, G.H. Waller, Y. Liu, M. Liu, C.-P. Wong, 3D Nitrogen-doped graphene prepared by pyrolysis of graphene oxide with polypyrrole for electrocatalysis of oxygen reduction reaction, *Nano Energy* 2 (2) (2013) 241–248.
- [86] J. Pels, F. Kapteijn, J. Moulijn, Q. Zhu, K. Thomas, Evolution of nitrogen functionalities in carbonaceous materials during pyrolysis, *Carbon* 33 (11) (1995) 1641–1653.
- [87] R. Sánchez-Salas, S. Kashina, R. Galindo, A.K. Cuentas-Gallegos, N. Rayón-López, M. Miranda-Hernandez, R. Fuentes-Ramírez, F. López-Urías, E. Muñoz-Sandoval, Effect of pyrrolic-N defects on the capacitance and magnetization of nitrogen-doped multiwalled carbon nanotubes, *Carbon* 183 (2021) 743–762.
- [88] W. Shen, C. Wang, Q. Xu, H. Liu, Y. Wang, Nitrogen-doping-induced defects of a carbon coating layer facilitate Na-storage in electrode materials, *Adv. Energy Mater.* 5 (1) (2015) 1400982.
- [89] Y.-C. Lin, P.-Y. Teng, C.-H. Yeh, M. Koshino, P.-W. Chiu, K. Suenaga, Structural and chemical dynamics of pyridinic-nitrogen defects in graphene, *Nano Lett.* 15 (11) (2015) 7408–7413.
- [90] J.-H. Wee, C.H. Kim, H.-S. Lee, G.B. Choi, D.-W. Kim, C.-M. Yang, Y.A. Kim, Enriched pyridinic nitrogen atoms at nanoholes of carbon nanohorns for efficient oxygen reduction, *Sci. Rep.* 9 (1) (2019) 20170.
- [91] R. Mohan, A. Modak, A. Schechter, A comparative study of plasma-treated oxygen-doped single-walled and multiwalled carbon nanotubes as electrocatalyst for efficient oxygen reduction reaction, *ACS Sustainable Chem. Eng.* 7 (13) (2019) 11396–11406.
- [92] K. Choi, S. Kim, Theoretical study of oxygen reduction reaction mechanism in metal-free carbon materials: defects, structural flexibility, and chemical reaction, *ACS Nano* 16 (10) (2022) 16394–16401.
- [93] J. Wang, C.-X. Zhao, J.-N. Liu, D. Ren, B.-Q. Li, J.-Q. Huang, Q. Zhang, Quantitative kinetic analysis on oxygen reduction reaction: A perspective, *Nano Mater. Sci.* 3 (3) (2021) 313–318.
- [94] D. Guo, R. Shibuya, C. Akiba, S. Saji, T. Kondo, J. Nakamura, Active sites of nitrogen-doped carbon materials for oxygen reduction reaction clarified using model catalysts, *Science* 351 (6271) (2016) 361–365.
- [95] W.J. Lee, U.N. Maiti, J.M. Lee, J. Lim, T.H. Han, S.O. Kim, Nitrogen-doped carbon nanotubes and graphene composite structures for energy and catalytic applications, *Chem. Commun.* 50 (52) (2014) 6818–6830.
- [96] N.D.K. Tu, S.O. Park, J. Park, Y. Kim, S.K. Kwak, S.J. Kang, Pyridinic-nitrogen-containing carbon cathode: efficient electrocatalyst for seawater batteries, *ACS Appl. Energy Mater.* 3 (2) (2020) 1602–1608.
- [97] F. Zhang, J. Miao, W. Liu, D. Xu, X. Li, Heteroatom embedded graphene-like structure anchored on porous biochar as efficient metal-free catalyst for ORR, *Int. J. Hydrogen Energy* 44 (59) (2019) 30986–30998.
- [98] T. Lu, X. Hu, J. He, R. Li, J. Gao, Q. Lv, Z. Yang, S. Cui, C. Huang, Aqueous/solid state Zn-air batteries based on N doped graphdiyne as efficient metal-free bifunctional catalyst, *Nano Energy* 85 (2021) 106024.
- [99] G. Chao, L. Zhang, D. Wang, S. Chen, H. Guo, K. Xu, W. Fan, T. Liu, Activation of graphitic nitrogen sites for boosting oxygen reduction, *Carbon* 159 (2020) 611–616.
- [100] X. Lu, D. Wang, L. Ge, L. Xiao, H. Zhang, L. Liu, J. Zhang, M. An, P. Yang, Enriched graphitic N in nitrogen-doped graphene as a superior metal-free electrocatalyst for the oxygen reduction reaction, *New J. Chem.* 42 (24) (2018) 19665–19670.
- [101] O.L. Li, S. Chiba, Y. Wada, G. Panomsuwan, T. Ishizaki, Synthesis of graphitic-N and amino-N in nitrogen-doped carbon via a solution plasma process and exploration of their synergistic effect for advanced oxygen reduction reaction, *J. Mater. Chem. A* 5 (5) (2017) 2073–2082.
- [102] Z. Luo, S. Lim, Z. Tian, J. Shang, L. Lai, B. MacDonald, C. Fu, Z. Shen, T. Yu, J. Lin, Pyridinic N doped graphene: synthesis, electronic structure, and electrocatalytic property, *J. Mater. Chem.* 21 (22) (2011) 8038–8044.
- [103] J. Wu, L. Ma, R.M. Yadav, Y. Yang, X. Zhang, R. Vajtai, J. Lou, P.M. Ajayan, Nitrogen-doped graphene with pyridinic dominance as a highly active and stable electrocatalyst for oxygen reduction, *ACS Appl. Mater. Interfaces* 7 (27) (2015) 14763–14769.
- [104] H. Miao, S. Li, Z. Wang, S. Sun, M. Kuang, Z. Liu, J. Yuan, Enhancing the pyridinic N content of Nitrogen-doped graphene and improving its catalytic activity for oxygen reduction reaction, *Int. J. Hydrogen Energy* 42 (47) (2017) 28298–28308.
- [105] S.M. Hwang, J.S. Park, Y. Kim, W. Go, J. Han, Y. Kim, Y. Kim, Rechargeable seawater batteries—from concept to applications, *Adv. Mater.* 31 (20) (2019) 1804936.